Misaligned Spinning Binary Black Hole Mergers in Hot Magnetized Plasma

Federico Cattorini[1,2] , Sofia Maggioni[3], Bruno Giacomazzo[2,3,4] , Francesco Haardt[1,2,4] , Monica Colpi[2,3], and Stefano Covino[1,4]

[1] DiSAT, Università degli Studi dell'Insubria, Via Valleggio, 11, I-22100 Como, Italy; fcattorini@uninsubria.it
[2] INFN, Sezione di Milano-Bicocca, Piazza della Scienza 3, I-20126 Milano, Italy
[3] Dipartimento di Fisica G. Occhialini, Università di Milano-Bicocca, Piazza della Scienza 3, I-20126 Milano, Italy
[4] INAF, Osservatorio Astronomico di Brera, Via E. Bianchi 46, I-23807 Merate, Italy

Abstract

We present general relativistic magnetohydrodynamical simulations of equal-mass spinning black hole binary mergers embedded in a magnetized gas cloud. We focus on the effect of the spin orientation relative to the orbital angular momentum on the flow dynamics, mass accretion rate, and Poynting luminosity. We find that, across the inspiral, the gas accreting onto the individual black holes concentrates into disklike overdensities whose angular momenta are oriented toward the spin axes and that persist until merger. We identify quasiperiodic modulations occurring in the mass accretion rate at the level of ∼1%–20%, evolving in parallel with the gravitational-wave chirp. The similarity between the accretion rate time series and the gravitational strain is a consequence of the interplay between strong, dynamical gravitational fields and magnetic fields in the vicinity of the inspiraling black holes. This result suggests that quasiperiodicity in the premerger accretion rate of massive binaries is not exclusive of environments in which the black holes are embedded in a circumbinary accretion disk and could provide an additional useful signature of electromagnetic emission concurrent to low-frequency gravitational-wave detection.

Unified Astronomy Thesaurus concepts: General relativity (641); Gravitational waves (678); Supermassive black holes (1663); Black hole physics (159); Gravitational wave sources (677); Magnetohydrodynamical simulations (1966); Rotating black holes (1406)

1. Introduction

Most galaxies are believed to host a central massive black hole (MBH), and, as a result of galaxy mergers, MBH binaries (MBHBs) are expected to form (see, e.g., Colpi 2014, for a review). The MBHBs are understood to be the loudest sources of low-frequency gravitational waves (GW), whose detection will be one of the main scientific goals of future spaceborne interferometers such as LISA (Amaro-Seoane et al. 2017).

Since MBHB mergers are anticipated to occur in gas-rich environments, we expect these events to be sources of conspicuous electromagnetic (EM) radiation as well, yielding unique opportunities for multimessenger detections (Bogdanovic et al. 2021). In order to understand the mechanisms that may give rise to such EM counterparts, it is crucial to confront future multimessenger observations with magnetohydrodynamical models of the gas around spinning MBHs in proximity and after merger. Due to the complexity of the underlying phenomena, this modeling needs to be mostly numerical.

Over the last decade, many numerical studies explored the evolution of gas around MBHBs, progressively adding the layers of physics that are needed to investigate the physical mechanisms that govern the observable signatures of an MBHB inspiral and merger. There is still a large uncertainty about the type of environment found in the proximity of merging MBHs; so far, these extreme events have been examined in two limiting scenarios, i.e., the (i) circumbinary disk (CBD) and (ii) gas cloud model. The former has been the subject of numerous numerical investigations and explored by

several theoretical groups with different techniques: Newtonian (and pseudo-Newtonian) viscous hydrodynamics (MacFadyen & Milosavljević 2008; D'Orazio et al. 2016; Tang et al. 2018; Tiede et al. 2020) and magnetohydrodynamics (MHD; Shi et al. 2012; Shi & Krolik 2016), MHD evolution over post-Newtonian spacetime metrics (Noble et al. 2012; Zilhão et al. 2015; Bowen et al. 2017, 2018; Noble et al. 2021), and fully general relativistic magnetohydrodynamic (GRMHD) simulations (Farris et al. 2012; Gold et al. 2014a, 2014b). These works studied the CBD response to MBHB inspirals (Noble et al. 2012), the mass feeding to individual "mini-disks" around inspiraling MBHs (Bowen et al. 2017, 2018), and the EM radiation emerging from these systems employing ray-tracing techniques (D'Ascoli et al. 2018; Gutiérrez et al. 2021). More recently, the impact of the spins of individual BHs on the dynamics of mini-disks was explored by Paschalidis et al. (2021) in full GR and by Armengol et al. (2021) employing an approximate metric for the spacetime evolution (Combi et al. 2021a, 2022).

If the accretion flow surrounding the binary is radiatively inefficient, a gas cloud scenario is a fair approximation of the physical conditions of matter in the vicinity of the BHs (Bogdanović et al. 2011). In the first numerical studies of such a scenario (Farris et al. 2010; Bode et al. 2012), the late inspiral and merger take place in a hot, homogeneous cloud in which the gas is either at rest or moving relative to the binary. Giacomazzo et al. (2012) pioneered the theoretical study of merging binaries in magnetized gas clouds using full GRMHD techniques. A later development by Kelly et al. (2017) explored how BHB mergers are affected by different values of the gas magnetization parameterized by the magnetic-to-gas pressure ratio $\beta^{-1} = p_{\mathrm{mag}}/p_{\mathrm{gas}}$. These works both considered merging equal-mass, nonspinning BHBs immersed in a diffuse hot gas

Table 1
BHB Initial Data Parameters and Derived Quantities in Code Units of the GRMHD Runs

Run	a_0 (M)	p_x	p_y	$\hat{a}_1$	$\hat{a}_2$	t_{merger} (M)	M_{rem}	$a_{z,rem}$	v_{kick} (km s^{-1} M_6)
UU		4.62e-4	8.19e-2	(0.0, 0.0, 0.6)	(0.0, 0.0, 0.6)	2529	0.951	0.858	⋯
UD		5.16e-4	8.43e-2	(0.0, 0.0, −0.6)	(0.0, 0.0, 0.6)	1989	0.951	0.622	261
DD	12.162	6.24e-4	8.73e-2	(0.0, 0.0, −0.6)	(0.0, 0.0, −0.6)	1452	0.964	0.459	⋯
UUMIS		4.6e-4	8.24e-2	(−0.42, 0.0, 0.42)	(0.42, 0.0, 0.42)	2401	0.935	0.811	1739
UDMIS		5.16e-4	8.43e-2	(−0.42, 0.0, −0.42)	(0.42, 0.0, 0.42)	2008	0.951	0.688	797

Note. Velocities are normalized to a binary system with total mass $M = 10^6 \, M_\odot$, and $M_6 \equiv M/10^6 \, M_\odot$.
Initial puncture separation a_0 and linear momentum components p_x and p_y, dimensionless spin vectors $\hat{a}_i = (a_{i,x}, a_{i,y}, a_{i,z})$ of each BH, merger time t_{merger}, remnant mass M_{rem}, z-component of the remnant spin parameter $a_{z,rem}$, and remnant kick velocity v_{kick} in kilometers per second

initially threaded by a uniform magnetic field aligned with the orbital angular momentum and examined the evolution of the mass accretion rate and the development of EM energy as Poynting flux. The aftermath of the merger was further investigated by Kelly et al. (2021), who focused on the steady-state behavior of the magnetized gas around a postmerger Kerr BH.

In Cattorini et al. (2021, hereafter Paper I), we extended the analysis of Giacomazzo et al. (2012) and Kelly et al. (2017) and performed the first simulations of equal-mass binaries of merging spinning BHs. We covered a range of initially uniform, moderately magnetized fluids with different initial values of β^{-1}. For each value of β^{-1}, we analyzed distinct spin configurations defined by the adimensional spin parameters $a = a_z = (0, \, 0.3, \, 0.6)$ and explored the dependence of the accretion rate $\dot{M}$ and Poynting luminosity L_{Poynt} on the magnitude of a. We found that, for a given initial value of β^{-1}, spin exerts a suppressing effect on the mass accretion rate; conversely, the postmerger peak Poynting luminosity of spinning BHB remnants can be enhanced by up to a factor of ~ 2.5. All configurations examined in Paper I considered binaries of spinning BHs with both spins aligned with the orbital angular momentum L_{orb}. Recent work by Kelly et al. (2021) and Ressler et al. (2021) began to explore the effect of magnetic field orientation with respect to the spin axis of a single accreting BH, e.g., varying the angle θ_B between the asymptotic magnetic field and the BH spin direction and investigating the sensitivity on θ_B of the Poynting luminosity L_{Poynt} and the accretion rate $\dot{M}$.

In this Letter, we present the first GRMHD simulations of the spinning binaries of BHs with spins either aligned, antialigned, or misaligned with the orbital angular momentum, investigating how the spin inclination modifies the magneto-hydrodynamical behavior of the plasma during the binary late inspiral and merger. As in Paper I, the simulations presented here aim at extracting physically relevant information that can help improve our understanding of hot accretion flows onto merging MBHBs. Also, we explore the effects of individual spin orientation in a binary system in order to determine how it affects the accretion flow and the properties of the emitted jet.

2. Numerical Methods

The details of the numerical setup employed for running the simulation presented here are thoroughly discussed in Paper I. Below, we limit ourselves to a rapid overview of the mathematical and computational techniques adopted in the present work. Throughout the paper, we use geometrized units, where $G = c = 1$.

2.1. Spacetime and Matter Fields Evolution

The simulations presented in this Letter are built upon the same configuration presented in Paper I. They were run with the `Einstein Toolkit`[56] framework (Löffler et al. 2012) using the "moving puncture" formalism (Campanelli et al. 2006; van Meter et al. 2006) and performing full GR evolution of both the spacetime metric and the magnetohydrodynamic fields. The spacetime metric is evolved via the `McLachlan` (Husa et al. 2006; Brown et al. 2009) thorn using the BSSNOK formulation (see, e.g., Shibata & Nakamura 1995; Baumgarte & Shapiro 1998). The MHD equations are solved in a flux-conservative formulation by the `IllinoisGRMHD` thorn (Noble et al. 2006; Etienne et al. 2015). The divergence-free property of the magnetic field is guaranteed with the evolution of the vector and scalar potentials in the "generalized" Lorenz gauge, and the MHD equations are solved in the ideal MHD limit; i.e., we consider a perfectly conducting medium in which Maxwell's equations reduce to $\nabla_\nu F^* \mu\nu = 0$. All binary evolutions are carried out on adaptive mesh refinement grids provided by the `Carpet` driver (Schnetter et al. 2004). We calculate the gas accretion rate using the thorn `Outflow` (Haas 2009), which measures the rest-mass density flow across the BH apparent horizons. The gravitational radiation generated during the late inspiral, merger, and ringdown is computed with the `WeylScal4` thorn via the Weyl curvature scalar Ψ_4, calculated given the fiducial tetrad of Baker et al. (2002).

2.2. Initial Conditions

The initial data of the simulations presented here were chosen consistently with Paper I. Since matter accretion tends to equalize the binary component masses, we have chosen to evolve equal-mass systems (Farris et al. 2014; Duffell et al. 2020). We perform a set of five runs (see Table 1). Each run evolves an equal-mass binary immersed in a uniform polytropic fluid ($p_0 = \kappa \rho_0^\Gamma$, with $\rho_0 = 1$, $\kappa = 0.2$, and $\Gamma = 4/3$), which is threaded by an initially uniform magnetic field aligned with the orbital angular momentum. The gas is initially at rest with respect to the binary. The total mass of the system in code units is set to be $M = 1$; the mass of each BH is $M/2$, and we assume the total mass of the gas to be negligible (i.e., we evolve Einstein's field equations in vacuum). The initial value of the magnetic field is chosen so that the initial magnetic-to-gas pressure is $\beta_0^{-1} \equiv p_{mag,0}/p_{gas,0} = 0.31$.

All simulations employ 11 refinement levels, with a resolution of $1/56 \, M$ on the finest grid, covering the apparent
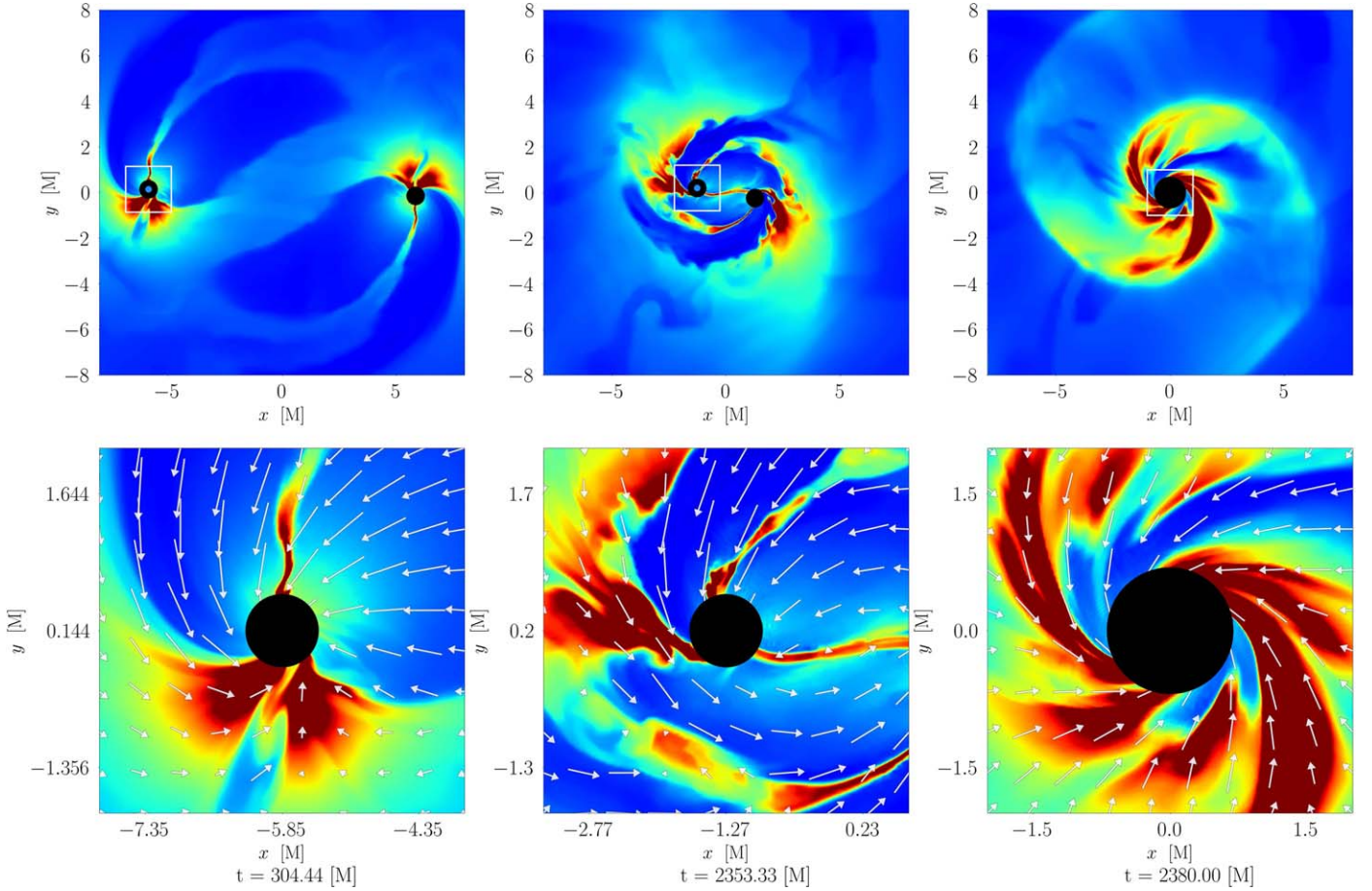

Figure 1. Top row: evolution of the rest-mass density ρ (normalized to its initial value ρ_0) on the xy-plane for the `UUMIS` configuration ($\hat{a}_1 = (-0.42, 0, +0.42)$, $\hat{a}_2 = (+0.42, 0, +0.42)$, $\beta_0^{-1} = 0.31$); snapshots were taken, respectively, after ~one orbit (left), after ~11 orbits (center), and at the time of merger (right). Bottom row: close-ups at the same epochs as the top panels of the region in the vicinity of the first BH's apparent horizon (left and middle panels) and of the remnant BH (right panel). Arrows denote velocity vectors. The black circles denote the interior of the apparent horizons. In the top panel, a colored dot is added inside the BH with initial spin $\hat{a}_1$.

horizon radius of each BH with ~20 grid points. In accordance with Paper I, the binaries are initialized on quasi-circular orbits at an initial separation $a_0 \approx 12\,M$. The adimensional spins in each run have the same magnitude, $a_1 = a_2 = 0.6$. In configuration `UU` (`DD`), both spins are aligned (antialigned) with the orbital angular momentum L_{orb}; in configuration `UD`, one spin is aligned, and the other is antialigned with L_{orb}; and in configurations `UUMIS` and `UDMIS`, the spins are misaligned with L_{orb}. In Table 1, we display the initial puncture positions, momenta, and spins of our five runs, along with merger times t_{merger}, remnant spins a_{rem}, and kick velocities v_{kick} (when present).

3. Results

To investigate the effects of spin orientation on the accretion flows, we study the evolution of the rest-mass density, velocity, and magnetic-to-gas pressure fields; the mass accretion rate onto the BH horizons; and the emitted Poynting luminosity as diagnostics.

3.1. MHD Fields Evolution

In the top row of Figure 1, we display the evolution of the rest-mass density ρ (normalized to its initial value ρ_0) on the xy-plane for the `UUMIS` configuration ($\hat{a}_1 = (-0.42, 0, +0.42)$,

$\hat{a}_2 = (+0.42, 0, +0.42)$). We choose the `UUMIS` configuration as our representative model because it is a clear demonstration of the effects of spin on the accretion rate and Poynting luminosity (see Section 3.4). A colored dot was added inside the BH with initial spin $\hat{a}_1$. In the bottom row, we show close-ups of the region in the vicinity of the first BH's apparent horizon (left and middle panels) and the remnant BH (right panel). White arrows denote the velocity vectors of the fluid.

The behavior of the plasma in the equatorial plane resembles the evolution of the magnetized simulations of Giacomazzo et al. (2012), Kelly et al. (2017), and Paper I. The main differences with respect to those configurations appear in the field evolution in the polar plane. In Figure 2, we display 2D slices in the xz-plane representing the evolution of the rest-mass density field ρ/ρ_0 (top row), velocity field (middle row), and magnetic-to-gas pressure field β^{-1} (bottom row) for our `UUMIS` run. The simulation begins ~2400 M (~11 orbits) before merger, with an initially uniform gas and a uniform magnetic field directed along the orbital axis. After a time as short as one orbit, matter starts to concentrate around each BH, forming two overdensities distributed in planar disklike structures (see also Giacomazzo et al. 2012; Kelly et al. 2017; Figure 1 in Paper I). However, unlike previous results of nonspinning and aligned-spin BHBs, the flow structure around the BHs is approximately orthogonal to the spin axes (Figure 2,
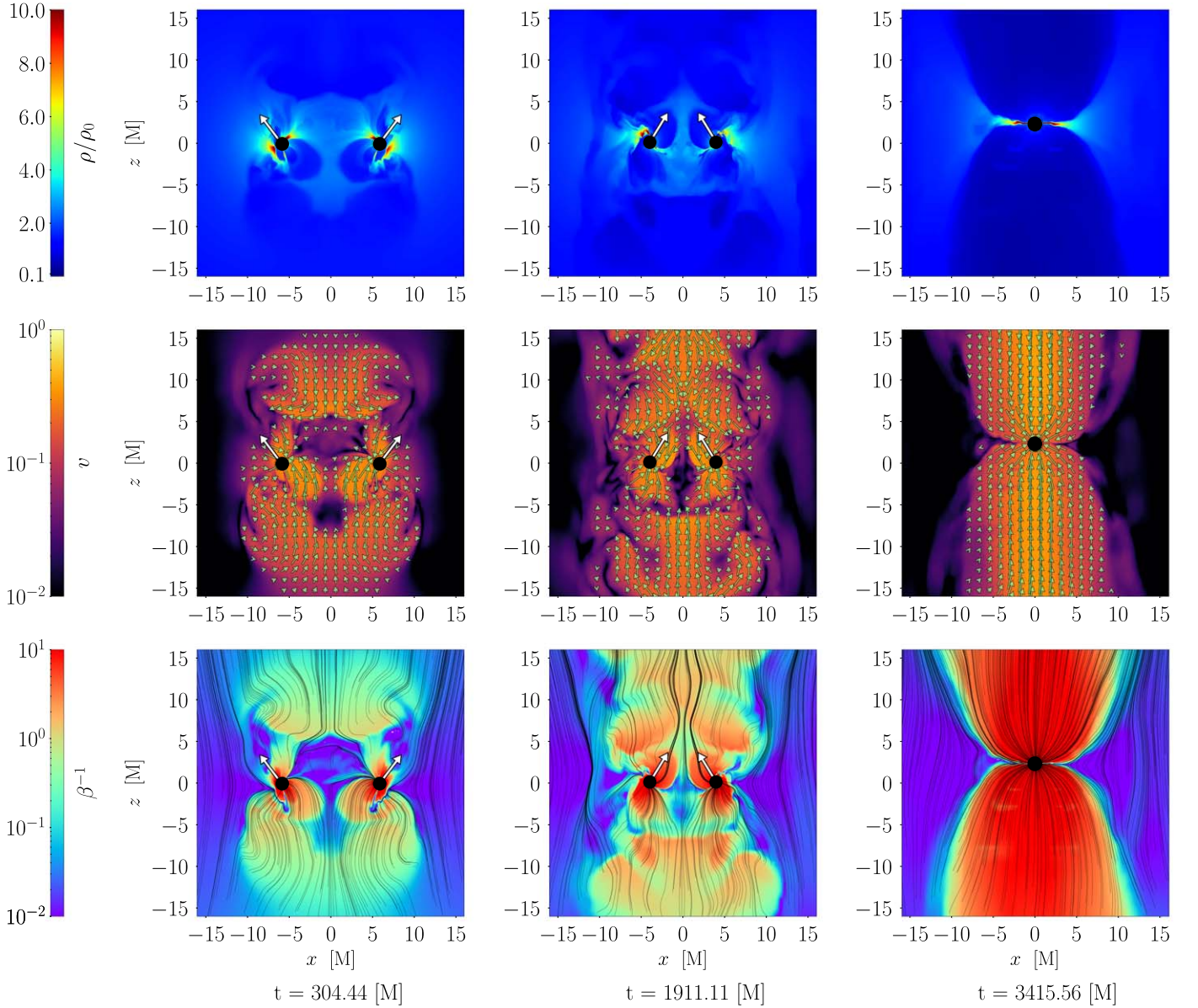
Figure 2. Top row: evolution of the rest-mass density ρ (normalized to its initial value ρ_0) on the xz-plane. Middle row: evolution of the fluid velocity field $\vec{v}$ on the xz-plane. The color bar refers to the magnitude $v = (v_x^2 + v_z^2)^{1/2}$. Arrows refer to the gas velocity field. Bottom row: evolution of the magnetic field lines on the xz-plane. The color bar refers to the magnetic-to-gas pressure ratio β^{-1}. The regions inside the BH horizons have been masked out. All snapshots refer to our UUMIS configuration ($\hat{a}_1 = (-0.42, 0, +0.42)$, $\hat{a}_2 = (+0.42, 0, +0.42)$, $\beta_0^{-1} = 0.31$); snapshots were taken, respectively, after ∼one orbit (left column), after ∼eight orbits (middle column), and at a time equal to ∼1000 M after merger (right column). The white arrows over the BHs in the left and middle columns denote spin vectors.

first row, left and middle panels). These structures persist until merger, when matter settles into a disklike overdensity around the Kerr BH remnant, which weakly oscillates around the orbital plane (Figure 2, first row, right panel), and is dragged by the BH remnant, which is recoiling with a velocity $v_{\text{kick}} \approx 1700\,M_6\,\text{km s}^{-1}$ in the direction of the z-axis.

The inclination of the disklike overdensities can be understood in terms of the magnetic field behavior in the proximity of the horizons. As the BHs orbit around each other, the magnetic field lines accumulate near the horizons and are oriented toward the spin axis of each BH (Figure 2, third row, left and middle panels), leading to the formation of magnetically dominated funnels, which we call "protojets"[7]

---

[7] We define protojets as magnetically dominated regions with a strong, localized Poynting flux, in which the net fluid flow is directed inward.

following Kelly et al. (2021). We find that the smaller protojets emerging from the individual Kerr BHs are always oriented toward the BH spin direction at distances $\lesssim 5\,M$, whereas, at larger radii, the protojets are aligned to the orbital (z-)axis. This effect is in accordance with the results of simulations of individual postmerger Kerr BHs by Kelly et al. (2021). These regions eventually merge and form a protojet collimated in the polar direction (Figure 2, third row, right panel).

3.2. Mass Accretion Rate

The rest-mass flux across the horizon of each BH is computed by the Outflow thorn (Haas 2009). In the top panels of Figure 3, we display the time evolution of the mass accretion rate $\dot{M}$ for our five configurations. The values of $\dot{M}$ are in units of solar masses per year, normalized for a binary
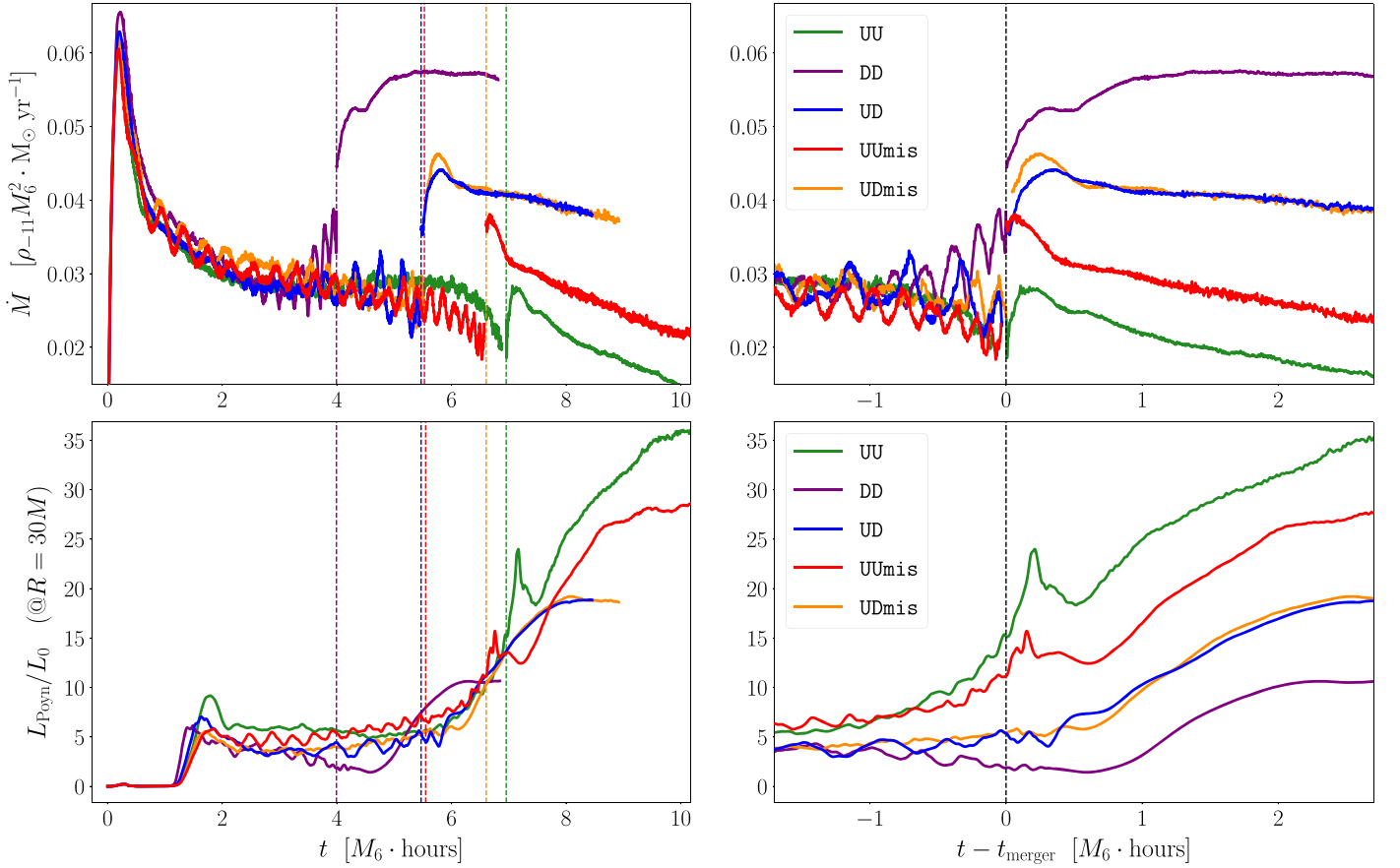
Figure 3. Top left: time-dependent accretion rates $\dot{M}$ in units of solar masses per year for the five configurations. The magnitudes of $\dot{M}$ are scaled to a binary of total mass $10^6\,M_\odot$ and a gas with an initial uniform rest-mass density $\rho = 10^{-11}\,\mathrm{g\,cm^{-3}}$. The premerger accretion rate is calculated onto both BH horizons; the postmerger accretion rate is calculated onto the remnant Kerr BH horizon. The dashed lines mark the merger times, and colors highlight the different configurations. Top right: comparison of $\dot{M}$ in the late inspiral, merger, and postmerger stages; time is rescaled with the merger time t_{merger}. Bottom left: time evolution of the Poynting luminosity L_{Poynt} for the five configurations. The luminosity is extracted on a sphere of radius $R_{\mathrm{ext}} = 30\,M$ centered on the origin of the system. The values of L_{Poynt} are in units of $L_0 \equiv 2.347 \times 10^{43}\rho_{-11}M_6^2\ \mathrm{erg\,s^{-1}}$, with $M_6 \equiv M/10^6\,M_\odot$, and $\rho_{-11} \equiv \rho/10^{11}\,\mathrm{g\,cm^{-3}}$. Bottom right: comparison of L_{Poynt} in the late inspiral, merger, and postmerger stages.

system of total mass $10^6\,M_\odot$ immersed in a plasma with initial density $10^{-11}\,\mathrm{g\,cm^{-3}}$. In the left panel, the dashed lines mark the time of merger for each configuration. In the right panel, we compare the accretion rates of the five runs in the late inspiral, merger, and postmerger stages; the time axis is aligned by the merger time of the binary t_{merger}.

In Paper I, we showed that higher values of the spin parameter result in a suppressing effect on $\dot{M}$. Analogous behavior is observed in our current set of simulations; run UU (which results in a Kerr BH remnant with spin parameter $a_{\mathrm{rem}} \sim 0.86$) has the lowest postmerger accretion rate ($\dot{M}_{\mathrm{UU}} \sim 0.15\ \rho_{-11}M_6^2\ M_\odot\,\mathrm{yr^{-1}}$), whereas run DD ($a_{\mathrm{rem}} \sim 0.46$) reaches the highest postmerger accretion rate ($\dot{M}_{\mathrm{DD}} \sim 0.6\ \rho_{-11}M_6^2\ M_\odot\,\mathrm{yr^{-1}}$). Other configurations exhibit in between values of $\dot{M}$. In general, a higher postmerger spin results in a lower accretion rate.

3.3. Poynting Luminosity

In Paper I, we investigated how the features of the EM Poynting luminosity L_{Poynt} relate to the initial magnetic-to-gas pressure β_0^{-1} and BH spins. In agreement with the results of Kelly et al. (2017), we observed that configurations with the same spin reach approximately the same value of L_{Poynt},

regardless of β_0^{-1}. However, we found that the peak Poynting luminosity, which is reached shortly after merger, is particularly dependent on the magnitude of the remnant's spin parameter. We show in the bottom panels of Figure 3 the time evolution of L_{Poynt} for our five runs. The values of L_{Poynt} are expressed in units of $L_0 \equiv 2.347 \times 10^{43}\rho_{-11}M_6^2\ \mathrm{erg\,s^{-1}}$ (see Paper I).

The main features of the Poynting luminosity light curves for the UU and UUMIS runs (see green and red curves in Figure 3, bottom panels) are similar to those displayed in Paper I: an initial steep rise (i), followed by a slow growth stage (ii) across the binary inspiral, a peak (iii) corresponding to merger, and a rapid climb (iv) toward a steady value (v). Configurations UD and UDMIS (blue and yellow curves, respectively) exhibit similar trends, except for the absence of evident peaks corresponding to binary mergers. Finally, configuration DD (purple curve) shows a moderate decrease across the inspiral and rapidly climbs over the merger and ringdown stages. As with the UD and UDMIS runs, configuration DD also does not feature a peak during merger.

We verified that the magnitude of the postmerger steady values of L_{Poynt} of our five configurations approximately scales with the spin parameter squared, a^2, in agreement with the Blandford–Znajek formula (Blandford & Znajek 1977). This
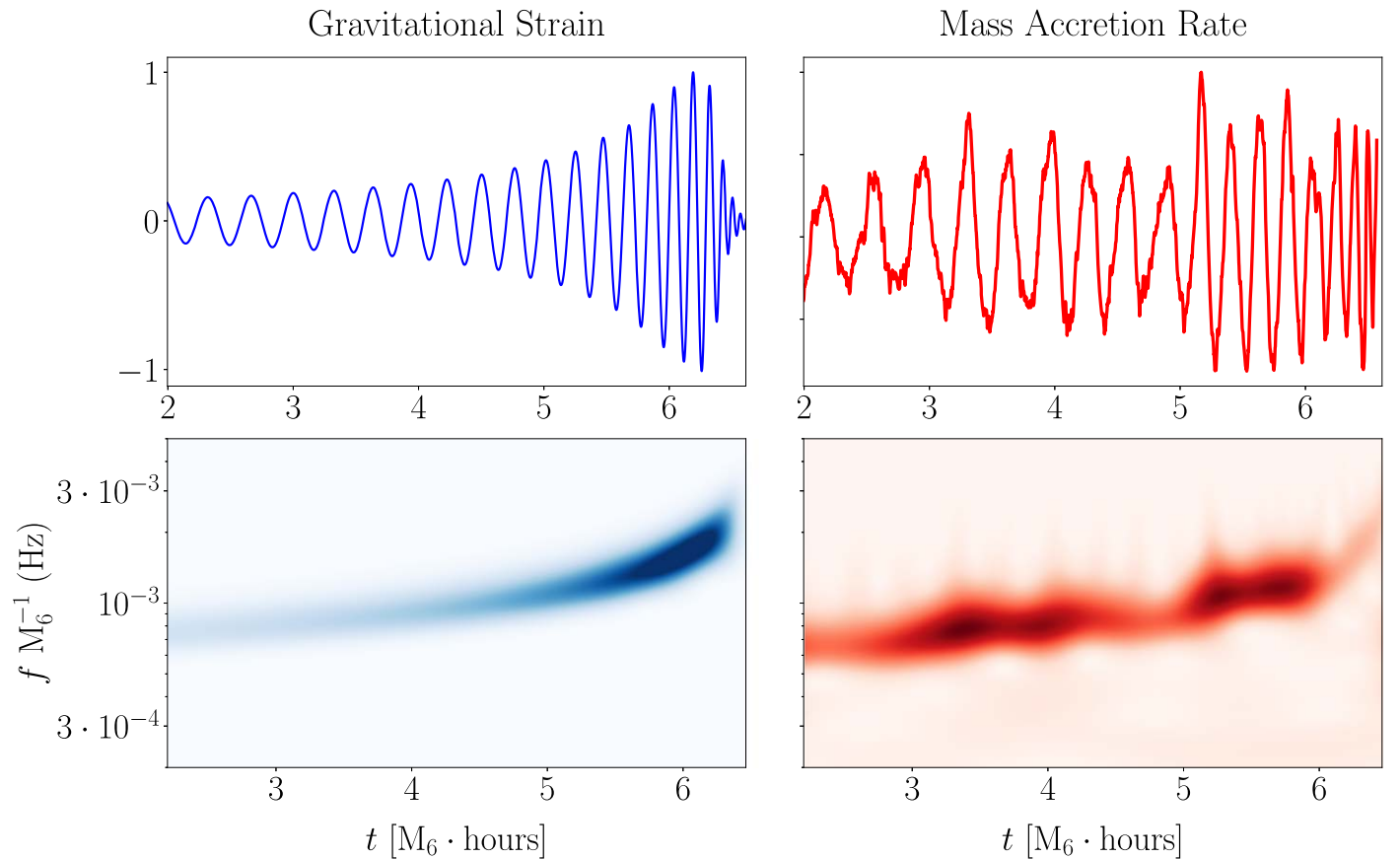
Figure 4. Top left: GW strain of the `UUMIS` run extracted via the Weyl scalar Ψ_4 with the `WeylScal4` thorn and normalized to its maximum value at merger. Top right: time-dependent premerger mass accretion rate $\dot{M}^* = \dot{M} - p_6$ over both BH horizons for the `UUMIS` run, also normalized to its maximum value. Bottom left: time-frequency representation of the GW strain via WPSD, showing the frequency increase of the signal over time. Bottom right: time-frequency representation of $\dot{M}^*$ via WPSD, showing a similarity with the GW strain in the frequency increase over time. Time and frequency units are normalized to a binary system with total mass $M = 10^6 \, M_\odot$, and $M_6 \equiv M/10^6 \, M_\odot$.

scaling will be the subject of a future investigation involving a broader family of spinning configurations.

3.4. Modulations

Over the last decade, a number of explorative works have reported that quasiperiodic features in the light curve of a MBHB system may arise thanks to the fueling-rate variability in the mini-disks around each BH due to the periodic interaction of the BHs with the inner edge of the CBD (Noble et al. 2012; Farris et al. 2014, 2015; Tang et al. 2018) or because of relativistic Doppler modulation (Haiman 2017). In our work, quasiperiodic variability is found in the time-dependent accretion rates for the five configurations presented (see Figure 3, top left panel). Similar—though weaker—oscillations are also present in the evolution of the Poynting luminosity (Figure 3, bottom left panel), but only when it is extracted on spheres of radii of 10 or 30 M; when L_{Poynt} is extracted at higher radii (in our cases, at 50, 80, and 100 M), its oscillatory behavior disappears, and the light curves across the inspiral are smooth. This is in agreement with simulations of nonspinning BHs carried out by Kelly et al. (2017; see their Figure 21). In what follows, we focus on the time variability of $\dot{M}(t)$, since it provides a more immediate correlate to detectable EM emission via accretion luminosity.

We observe that, over the last $\sim$10 orbits of the `UUMIS` configuration, the accretion rate displays a clear modulation,

with oscillations occurring with amplitude $\sim$10% the average rate. The amplitude of such oscillations is lowest for the `UU` run ($\sim$1%) and largest for the `UD` and `DD` runs ($\sim$20%).

In order to examine the harmonic connection of the premerger accretion rate with the chirping GW signal, we perform a wavelet power spectral density (WPSD) analysis (Chatterji et al. 2004). We fit the premerger accretion rate with a sixth-order polynomial p_6 and subtract it from $\dot{M}$ in order to remove the initial transient and the late decrease prior to merger. In Figure 4 (top row), we plot the gravitational strain computed via the Weyl scalar Ψ_4 (left) and the quantity $\dot{M}^* = \dot{M} - p_6$ (right) representing the premerger accretion rate for the `UUMIS` run, both normalized to their maximum value. To investigate the time-frequency behavior of $\dot{M}^*$, we compute its WPSD and compare it to the WPSD of the GW strain (Figure 4, bottom row). Our main result is that the $\dot{M}^*$ time series (right panel) oscillates with a frequency increment that closely resembles the increase of the characteristic GW chirp frequency with time (left panel).

The occurrence of modulations of the accretion rate on such short space and timescales is remarkable, for it can possibly be translated into quasiperiodic oscillations in the EM light curve, allowing for the identification of an EM counterpart to the GW event. In general, the quasiperiodic modulations appear to be independent of the larger-scale structure of the binary gaseous environment and depend only upon the magnetohydrodynamic features of the accreting fluid near the horizons.

The mechanism behind these fluctuations is not completely clear and will be the subject of future investigation. Still, we verified that no modulation in $\dot{M}$ is present whenever the fluid is not initially threaded by a magnetic field, hence suggesting that such modulations arise as a result of the interplay of magnetic fields and strong, dynamical gravitational fields.

4. Conclusions

We have presented the first GRMHD simulations of equal-mass spinning BHB mergers with spins misaligned with respect to the orbital angular momentum. We performed a suite of five simulations of BHBs initially immersed in a uniform gas cloud with a uniform magnetic field aligned with the binary orbital angular momentum $L_{\rm orb}$. Each configuration evolves BHs with spins of the same magnitude but differing in orientation relative to $L_{\rm orb}$. In agreement with previous results from Paper I, we found that a higher postmerger spin of the remnant BH corresponds to lower mass accretion rates onto the BH horizon, and that the postmerger value of the Poynting luminosity is proportional to the square of the spin parameter of the newly formed BH. We discovered the occurrence of quasiperiodic oscillations in the mass accretion rate—and, possibly, in the emitted EM radiation—during the inspiral phase and found that the oscillation frequency of the accretion rate increases with the time to merger, mimicking the gravitational chirp. This similarity seemingly arises as a consequence of the interplay of the magnetic field in the vicinity of a merging binary and the spins of the individual BHs. This finding suggests that quasiperiodicities in the premerger accretion rate are not exclusive of environments in which a BHB is embedded in a circumbinary accretion disk. Such oscillations may give rise to quasiperiodic EM emission in the X-ray band, which could potentially be detected by the future Athena mission (Piro et al. 2021), thus providing a useful signature of the EM signal concurrent to the gravitational emission of merging MBHBs.

ORCID iDs

Federico Cattorini https://orcid.org/0000-0002-3907-9583
Bruno Giacomazzo https://orcid.org/0000-0002-6947-4023
Francesco Haardt https://orcid.org/0000-0003-3291-3704
Stefano Covino https://orcid.org/0000-0001-9078-5507

References

Amaro-Seoane, P., Audley, H., Babak, S., et al. 2017, arXiv:1702.00786
Armengol, F. G. L., Combi, L., Campanelli, M., et al. 2021, ApJ, 913, 16
Baker, J., Campanelli, M., & Lousto, C. O. 2002, PhRvD, 65, 044001
Baumgarte, T. W., & Shapiro, S. L. 1998, PhRvD, 59, 024007
Blandford, R. D., & Znajek, R. L. 1977, MNRAS, 179, 433
Bode, T., Bogdanović, T., Haas, R., et al. 2012, ApJ, 744, 45
Bogdanović, T., Bode, T., Haas, R., Laguna, P., & Shoemaker, D. 2011, CQGra, 28, 094020
Bogdanovic, T., Miller, M. C., & Blecha, L. 2021, arXiv:2109.03262
Bowen, D. B., Campanelli, M., Krolik, J. H., Mewes, V., & Noble, S. C. 2017, ApJ, 838, 42
Bowen, D. B., Mewes, V., Campanelli, M., et al. 2018, ApJL, 853, L17
Brown, D., Diener, P., Sarbach, O., Schnetter, E., & Tiglio, M. 2009, PhRvD, 79, 044023
Campanelli, M., Lousto, C. O., Marronetti, P., & Zlochower, Y. 2006, PhRvL, 96, 111101
Cattorini, F., Giacomazzo, B., Haardt, F., & Colpi, M. 2021, PhRvD, 103, 103022
Chatterji, S., Blackburn, L., Martin, G., & Katsavounidis, E. 2004, CQGra, 21, S1809
Colpi, M. 2014, SSRv, 183, 189
Combi, L., Armengol, F. G. L., Campanelli, M., et al. 2021a, PhRvD, 104, 044041
Combi, L., Lopez Armengol, F. G., Campanelli, M., et al. 2022, ApJ, 928, 187
D'Ascoli, S., Noble, S. C., Bowen, D. B., et al. 2018, ApJ, 865, 140
D'Orazio, D. J., Haiman, Z., Duffell, P., MacFadyen, A., & Farris, B. 2016, MNRAS, 459, 2379
Duffell, P. C., D'Orazio, D., Derdzinski, A., et al. 2020, ApJ, 901, 25
Etienne, Z. B., Paschalidis, V., Haas, R., Mösta, P., & Shapiro, S. L. 2015, CQGra, 32, 175009
Farris, B. D., Duffell, P., MacFadyen, A. I., & Haiman, Z. 2014, ApJ, 783, 134
Farris, B. D., Duffell, P., MacFadyen, A. I., & Haiman, Z. 2015, MNRAS, 446, L36
Farris, B. D., Gold, R., Paschalidis, V., Etienne, Z. B., & Shapiro, S. L. 2012, PhRvL, 109, 221102
Farris, B. D., Liu, Y. T., & Shapiro, S. L. 2010, PhRvD, 81, 084008
Giacomazzo, B., Baker, J. G., Miller, M. C., Reynolds, C. S., & van Meter, J. R. 2012, ApJL, 752, L15
Gold, R., Paschalidis, V., Etienne, Z. B., Shapiro, S. L., & Pfeiffer, H. P. 2014a, PhRvD, 89, 064060
Gold, R., Paschalidis, V., Ruiz, M., et al. 2014b, PhRvD, 90, 104030
Gutiérrez, E. M., Combi, L., Noble, S. C., et al. 2021, ApJ, 928, 137
Haas, R. 2009, Cactus Code Thorn Outflow https://bitbucket.org/einsteintoolkit/einsteinanalysis/src/master/Outflow/
Haiman, Z. 2017, PhRvD, 96, 023004
Husa, S., Hinder, I., & Lechner, C. 2006, CoPhC, 174, 983
Kelly, B. J., Baker, J. G., Etienne, Z. B., Giacomazzo, B., & Schnittman, J. 2017, PhRvD, 96, 123003
Kelly, B. J., Etienne, Z. B., Golomb, J., et al. 2021, PhRvD, 103, 063039
Löffler, F., Faber, J., Bentivegna, E., et al. 2012, CQGra, 29, 115001
MacFadyen, A. I., & Milosavljević, M. 2008, ApJ, 672, 83
Noble, S. C., Gammie, C. F., McKinney, J. C., & Zanna, L. D. 2006, ApJ, 641, 626
Noble, S. C., Krolik, J. H., Campanelli, M., et al. 2021, ApJ, 922, 175
Noble, S. C., Mundim, B. C., Nakano, H., et al. 2012, ApJ, 755, 51
Paschalidis, V., Bright, J., Ruiz, M., & Gold, R. 2021, ApJL, 910, L26
Piro, L., Ahlers, M., Coleiro, A., et al. 2021, arXiv:2110.15677
Ressler, S. M., Quataert, E., White, C. J., & Blaes, O. 2021, MNRAS, 504, 6076
Schnetter, E., Hawley, S. H., & Hawke, I. 2004, CQGra, 21, 1465
Shi, J.-M., & Krolik, J. H. 2016, ApJ, 832, 22
Shi, J.-M., Krolik, J. H., Lubow, S. H., & Hawley, J. F. 2012, ApJ, 749, 118
Shibata, M., & Nakamura, T. 1995, PhRvD, 52, 5428
Tang, Y., Haiman, Z., & MacFadyen, A. 2018, MNRAS, 476, 2249
Tiede, C., Zrake, J., MacFadyen, A., & Haiman, Z. 2020, ApJ, 900, 43
van Meter, J. R., Baker, J. G., Koppitz, M., & Choi, D.-I. 2006, PhRvD, 73, 124011
Zilhão, M., Noble, S. C., Campanelli, M., & Zlochower, Y. 2015, PhRvD, 91, 024034